Available online at www.sciencedirect.com
SCIENCE DIRECT®
Journal of Molecular Catalysis A: Chemical 228 (2005) 11–19
JOURNAL OF MOLECULAR CATALYSIS A: CHEMICAL
www.elsevier.com/locate/molcata

Physical and chemical properties of $Ce_{1-x}Zr_xO_2$ nanoparticles and $Ce_{1-x}Zr_xO_2(1\,1\,1)$ surfaces: synchrotron-based studies

J.A. Rodriguez[a,*], X. Wang[a], G. Liu[a], J.C. Hanson[a], J. Hrbek[a], C.H.F. Peden[b], A. Iglesias-Juez[c], M. Fernández-García[c]

[a] *Department of Chemistry, Brookhaven National Laboratory, Upton, NY 11973, USA*
[b] *Environmental Molecular Sciences Laboratory, Pacific Northwest National Laboratory, Richland, WA 99352, USA*
[c] *Instituto de Catálisis y Petroleoquímica, CSIC, Campus Cantoblanco, 28049 Madrid, Spain*

Available online 19 November 2004

Abstract

In this article, we review a series of studies that use synchrotron-based techniques (high-resolution photoemission, time-resolved X-ray diffraction (XRD), and X-ray absorption near-edge spectroscopy) to investigate the physical and chemical properties of $Ce_{1-x}Zr_xO_2$ nanoparticles and $Ce_{1-x}Zr_xO_2(1\,1\,1)$ surfaces ($x \leq 0.5$). CeO_2 and $Ce_{1-x}Zr_xO_2$ particles in sizes between 4 and 7 nm were synthesized using a novel microemulsion method. The results of XANES (O K-edge, Ce and Zr L_{III}-edges) indicate that the $Ce_{1-x}Zr_xO_2$ nanoparticles and $Ce_{1-x}Zr_xO_2(1\,1\,1)$ surfaces have very similar electronic properties. For these systems, the lattice constant decreased with increasing Zr content, varying from 5.4 Å in CeO_2 to 5.3 Å in $Ce_{0.5}Zr_{0.5}O_2$. Within the fluorite structure, the Zr atoms exhibited structural perturbations that led to different types of Zr–O distances and non-equivalent O atoms in the $Ce_{1-x}Zr_xO_2$ compounds. The $Ce_{1-x}Zr_xO_2$ nanoparticles were more reactive towards H_2 and SO_2 than the $Ce_{1-x}Zr_xO_2(1\,1\,1)$ surfaces. The $Ce_{1-x}Zr_xO_2(1\,1\,1)$ surfaces did not reduce in hydrogen at 300 °C. At temperatures above 250 °C, the $Ce_{1-x}Zr_xO_2$ nanoparticles reacted with H_2 and water evolved into gas phase. XANES showed the generation of Ce^{3+} cations without reduction of Zr^{4+}. There was an expansion in the unit cell of the reduced nanoparticles probably as a consequence of a partial $Ce^{4+} \rightarrow Ce^{3+}$ transformation and the sorption of hydrogen into the bulk of the material. S K-edge XANES spectra pointed to SO_4 as the main product of the adsorption of SO_2 on the $Ce_{1-x}Zr_xO_2$ nanoparticles and $Ce_{1-x}Zr_xO_2(1\,1\,1)$ surfaces. Full dissociation of SO_2 was seen on the nanoparticles but not on the $Ce_{1-x}Zr_xO_2(1\,1\,1)$ surfaces. The metal cations at corner and edge sites of the $Ce_{1-x}Zr_xO_2$ nanoparticles probably play a very important role in interactions with the H_2 and SO_2 molecules.

Keywords: High-resolution photoemission; Time-resolved X-ray diffraction; Nanoparticles

1. Introduction

Ceria (CeO_2) is an oxide with important applications in the control of environmental pollution [1,2]. One of the major efforts of environmental cleanup is focused on controlling the emission of toxic pollutants produced during the combustion of fuels in factories, power plants and automotive engines [1–3]. The so-called three-way catalysts (TWC's) are commonly used to reduce the emissions of CO, NO_x and hydrocarbons from automobile exhaust [3,4]. Due to its redox properties, CeO_2 is a key component in these catalysts [2,3,5]. Ceria-supported noble-metal catalysts are capable of storing oxygen under oxidizing conditions and release oxygen under reducing conditions via the facile conversion between Ce^{4+} and Ce^{3+} oxidation states [5]. Furthermore, ceria-based materials are also utilized in sorbents or catalysts for the destruction of SO_2 ($DeSO_x$ operations) [6,7]. Oxygen anion vacancies in ceria are considered to play an essential role in catalytic reactions [5–11]. The energetics of O vacancy creation/filling can be altered after doping ceria with a second metal [11–13].

The CeO_2–ZrO_2 system is one of the most studied mixed-metal oxides in the literature due to its important role in the operation of automotive catalysts [1–5]. To enhance the redox properties and thermal stability of pure ceria, zirconia

* Corresponding author. Tel.: +1 516 2822246; fax: +1 516 2825815.
E-mail address: rodrigez@bnl.gov (J.A. Rodriguez).

1381-1169/$ – see front matter © 2004 Elsevier B.V. All rights reserved.
doi:10.1016/j.molcata.2004.09.069

(ZrO_2) is often mixed as an additive to form solid solutions of the $Ce_{1-x}Zr_xO_2$ type ($x \leq 0.5$) [5,12]. Typically, cations are randomly distributed in a fluorite-type subcell, whereas the total symmetry is governed by the anion subcell [5,12]. For these materials, tetragonal and cubic structures are possible [5,12,14]. The focus has been on examining possible correlations between the $CeO_2 \leftrightarrow ZrO_2$ interactions and differences in the behavior of $Ce_{1-x}Zr_xO_2$ and CeO_2. The mechanisms for the doping effects of Zr remain uncertain and are still a matter of debate. It has been suggested that ceria structural modifications mediated by zirconia and zirconia-stabilized defects in ceria are responsible for the enhanced oxygen-storage capacity of ceria–zirconia mixed oxides [12,15,16]. Contributions from "electronic effects" (i.e. modifications in the chemical properties of the metal cations as a consequence of electronic perturbations) have been frequently dismissed, although it is clear that they cannot be ruled out [8,13].

Nano structures of oxides can have special chemical properties due to size-induced structural distortions and the presence of O vacancies [18]. This is an issue that needs further investigation. Recent studies have shown that nanoparticles of $Ce_{1-x}Zr_xO_2$ can be prepared by a novel microemulsion method that leads to highly homogeneous materials in terms of chemical composition (i.e. Ce, Zr distribution), having a narrow distribution of particle sizes [19,20]. The catalysts prepared in this way are very useful for studying the thermal stability of the $Ce_{1-x}Zr_xO_2$ system and aging treatments at high temperature [4,19,20]. In this article, we review a series of studies that use synchrotron-based techniques (high-resolution photoemission [8,21], time-resolved X-ray diffraction (XRD) [17] and X-ray absorption near-edge spectroscopy [8,17]) to investigate the structural and electronic properties of $Ce_{1-x}Zr_xO_2$ nanoparticles and $Ce_{1-x}Zr_xO_2$(1 1 1) surfaces. The chemisorption of H_2 and SO_2 are used to examine the chemical properties of the $Ce_{1-x}Zr_xO_2$ systems. The study has practical applications as hydrogen is one of the reducing agents present in exhaust gases of automotive engines [1–3]. It is known that adsorption of SO_2 affects the performance of TWC's used to control emissions of CO and NO_x [22] and, on the other hand, ceria-based catalysts are highly active for $DeSO_x$ operations [6,7].

2. Experimental methods

To prepare the $Ce_{1-x}Zr_x$ O_2 nanoparticles and $Ce_{1-x}Zr_x$ O_2(1 1 1) surfaces, we followed methods previously reported in the literature [19,20,23,24]. A microemulsion method [19,20] was used to synthesize nanoparticles with initial Ce:Zr atomic ratios of 9:1, 2:1 and 1:1 in the reacting mixtures [17]. $Ce_{1-x}Zr_xO_2$(1 1 1) ($x = 0.1$, 0.2 or 0.3) thin films (500–700 Å in thickness) were grown on a Y-stabilized ZrO_2(1 1 1) surface by oxygen-plasma assisted molecular-beam epitaxy [23,24].

The time-resolved X-ray diffraction results shown in Section 3 were collected on beam line X7B of the National Synchrotron Light Source (NSLS) at Brookhaven National Laboratory (BNL) [17,25]. Investigations at BNL have established the feasibility of conducting subminute, time-resolved XRD experiments when combining the high intensity of synchrotron radiation and new parallel data-collection devices [25]. A MAR345 detector was used to record the in situ XRD data. The typical time required for collecting an individual diffraction pattern was in the range of 0.5–2 min. The powder rings were integrated using the FIT2D code [26]. Rietveld refinements were performed with the program GSAS [27,28]. In this work, a whole profile refinement with the commercial Reflex package provided by Accelrys was employed to obtain the particle sizes, cell dimension, and lattice strain [18,31]. Here lattice strain was determined from the variation of peak width, and is an estimation of the stress, produced by imperfections and defects, in the crystal structure [29–31].

The photoemission studies described in Section 3 were performed in a ultrahigh-vacuum (UHV) chamber that forms part of the U7A beamline in the NSLS [8,21]. The UHV chamber (with a base pressure of $\sim 5 \times 10^{-10}$ Torr) is fitted with a hemispherical electron energy analyzer with multichannel detection, optics for low-energy electron diffraction (LEED), a residual gas analyzer (SRS-RGA), and a twin (Mg Kα and Al Kα) X-ray source. The combined energy resolution in the photoemission spectra was 0.3–0.4 eV [8,21].

The Ce and Zr L_{III}-edge and S K-edge XANES spectra presented in Section 3 were collected at the NSLS on beam line X19A in the "fluorescence-yield mode" using a boomerang-type flat crystal monochromator and a special reaction cell with a modified Stern–Heald–Lytle detector [7,8,17]. Beamline U7A was utilized to record the O K-edge spectra. This beamline is equipped with a toroidal-spherical grating monochromator. The O K-edge spectra were taken in the "electron-yield mode" by using a channeltron multiplier located near the sample surface [8,17]. The energy resolution at the L_{III} (Ce or Zr) and K (S or O) edges was close to 0.5 eV.

3. Results

3.1. Structural properties of the $Ce_{1-x}Zr_xO_2$ systems

Fig. 1 shows the structure of an ideal $Ce_{1-x}Zr_xO_2$(1 1 1) surface ($x < 0.4$). The top layer consists of O atoms, but within this layer there are holes that expose the Ce or Zr cations in the second layer. The $Ce_{1-x}Zr_xO_2$(1 1 1) thin films used in the present study possess a pure and single-crystalline phase, and these surfaces are oxygen-terminated and well ordered as evidenced by the results of several techniques for structural characterization (reflection high-energy electron diffraction, low-energy electron diffraction, X-ray photoelectron diffraction, X-ray diffraction, and Rutherford backscattering spectroscopy and channeling) [8,23,24]. In the $Ce_{1-x}Zr_xO_2$(1 1 1) thin films and the $Ce_{1-x}Zr_xO_2$ nanoparticles, the Ce ↔ Zr ex-

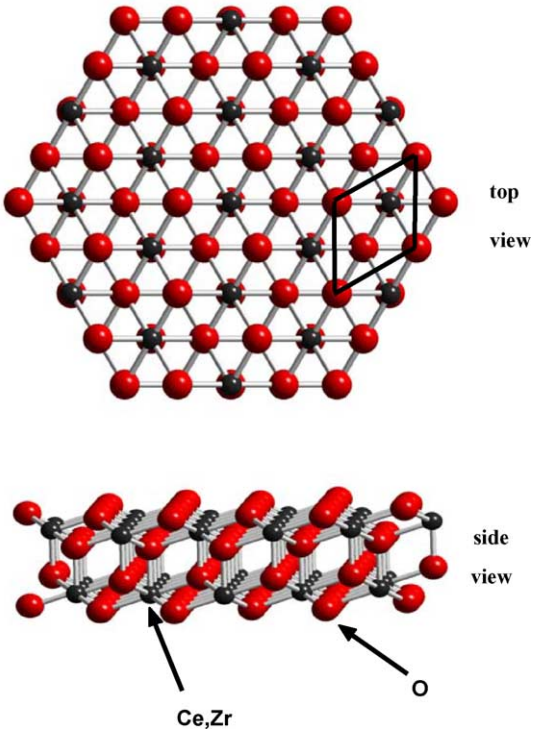

Fig. 1. Top and side views of an oxygen-terminated $Ce_{1-x}Zr_xO_2$(1 1 1) surface ($x < 0.4$). The large spheres represent O atoms, and the small spheres correspond to Ce or Zr atoms in a solid solution.

change led to a decrease in the lattice constant of the oxide [8,17,23], in agreement with reported XRD results for bulk powders of these compounds [32].

Fig. 2 shows time-resolved XRD results obtained after heating a sample of $Ce_{0.9}Zr_{0.1}O_2$ nanoparticles from 25 to 1000 °C [17]. When the temperature is raised, the diffraction lines clearly gain intensity and become better defined. No phase transformation is visible. These changes are a consequence of an increase in the size of the particles (sintering) at temperatures above 500 °C. This process was irreversible. Similar results were found for $Ce_{0.66}Zr_{0.33}O_2$ nanoparticles.

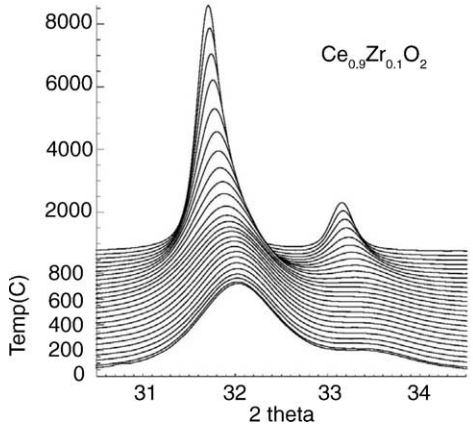

Fig. 2. Time-resolved XRD data for the heating of $Ce_{0.9}Zr_{0.1}O_2$ nanoparticles in air. Heating rate = 4.8 °C/min. λ = 0.8941 Å.

From the width of the diffraction lines, one can get a reasonable estimate of the average size of the CeO_2 and $Ce_{1-x}Zr_xO_2$ nanoparticles [29–31]. The top panel in Fig. 3 displays changes in size as a function of Zr concentration and temperature. Data for a limited number of temperatures have been published in ref. [17], but the corresponding new set in Fig. 3 is more extensive and the analysis of the XRD patterns was performed utilizing a more sophisticated approach (see Section 2) [31]. Initially, the particles have a size in the range of 5–7 nm. The size of the pure CeO_2 nanoparticles (~ 7 nm) is comparable to that obtained recently using a different synthetic method [14]. A similar size can be determined from images of transmission electron microscopy (TEM), which also show that there is no preferential orientation for the surface of the nanoparticles [18–20]. Around 600 °C, the size of the CeO_2 particles starts to increase and by 1000 °C is close to 25 nm. For the $Ce_{1-x}Zr_xO_2$ systems the sintering also starts near 600 °C, but the magnitude of the size increase seems to diminish when the content of Zr is raised [17]. The "extra" thermal stability could be a consequence of more dense packing of the atoms in the unit cell of the compound [17,31]. The trends in the top panel of Fig. 3 are important and consistent with the fact that the addition of zirconia to ceria enhances the thermal stability of automotive catalysts [2,4,15,32].

The strain in the $Ce_{1-x}Zr_xO_y$, nanoparticles as a function of Zr content and temperature is shown in the bottom panel

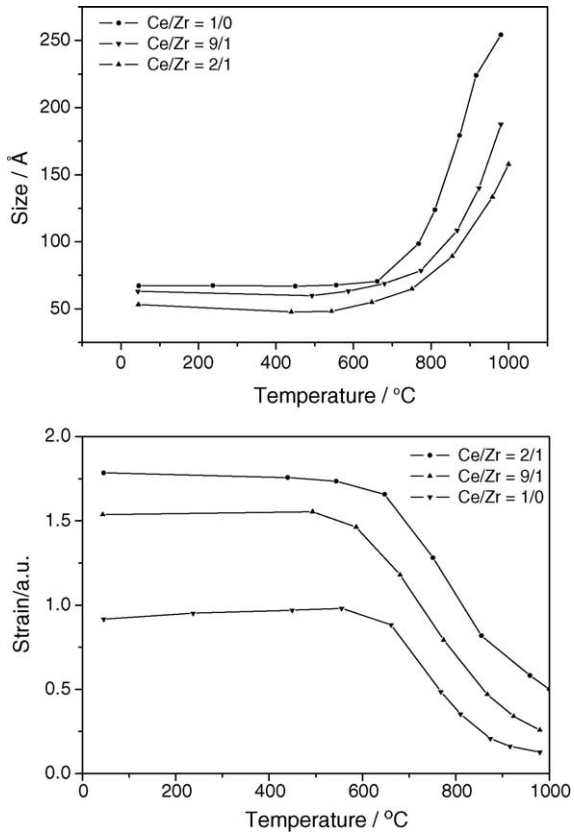

Fig. 3. Effects of heating on the size (top panel) and strain parameter of a series of $Ce_{1-x}Zr_xO_2$ ($x = 0$, 0.1, 0.33) nanoparticles.

of Fig. 3. Under ideal circumstances, the Bragg peaks in a powder diffractogram should appear as narrow well-defined symmetrical peaks. There are a number of sources of distortion that can result in significant peak broadening and asymmetry. The three main contributions to the line shape include instrumental broadening, crystalline size broadening, and strain broadening. Strain is a measurement of the lattice stress existing in the materials because of surface effects (differences in local symmetry and distances with respect to the bulk) and/or the crystal imperfections (O vacancies, other point defects, line defects and plane defects) [33]. Pure ceria nanoparticles exhibit a larger lattice strain when compared to bulk CeO_2. Clearly, the introduction of an alien species like Zr leads to extra forces that increase the strain in the lattice of the nanoparticles. There are important defect contributions to the strain that can be eliminated by annealing at high temperature and inducing sintering of the nanoparticles [34].

3.2. Electronic properties of the $Ce_{1-x}Zr_xO_2$ systems

The results of XANES (O K-edge, Ce and Zr L_{III}-edges) indicate that the $Ce_{1-x}Zr_xO_2$ nanoparticles and $Ce_{1-x}Zr_xO_2$(1 1 1) surfaces have very similar electronic properties [8,17]. The spectra for the Ce L_{III}-edge of the $Ce_{1-x}Zr_xO_2$ systems showed energies and the line shape reported for bulk CeO_2 [8,17]. Thus, the doping with Zr did not induce formation of a significant amount of Ce^{3+}. This is consistent with results of XRD for the nanoparticles, which show that the oxygen occupancy is essentially 100% (i.e. no O vacancies) [17,31], and with XPS and photoemission data for the $Ce_{1-x}Zr_xO_2$(1 1 1) surfaces [8].

Fig. 4 displays Zr L_{III}-edge spectra for bulk ZrO_2 and $Ce_{1-x}Zr_xO_2$ nanoparticles. The corresponding spectra for the $Ce_{1-x}Zr_xO_2$(1 1 1) surfaces are not shown, because they were very similar to those of the nanoparticles [8,17]. At the temperature in which the spectra were acquired (∼ 25 °C), a monoclinic crystal structure is the thermodynamically stable phase for ZrO_2 [8,35]. The Zr L_{III}-edge of this oxide is characterized by four distinctive features. The two main ones (a and b) correspond to electronic transitions from the occupied Zr 2p orbitals to the empty Zr 4d orbitals which are split into orbitals with t and e symmetry [36]. In oxides, the relative intensity of the a and b peaks depends strongly on the chemical environment around the Zr cations [36]. In the $Ce_{1-x}Zr_xO_2$ systems, the Zr atoms are in a pseudo-cubic environment [8,17] and the relative intensity of the b peak is stronger than observed for monoclinic ZrO_2 or for tetragonal Zr-doped Y_2O_3 [36]. The a and b peak separation in $Ce_{0.9}Zr_{0.1}O_2$ is ∼ 0.25 eV larger than in ZrO_2. As the concentration of zirconium in $Ce_{1-x}Zr_xO_2$ increases, the Zr L_{III}-edge line shape changes and becomes closer to that in pure ZrO_2 (bottom of Fig. 4).

Fig. 5 shows O K-edge XANES spectra for a series of $Ce_{1-x}Zr_xO_2$ nanoparticles [17], including reference spectra for bulk ZrO_2 and CeO_2. The features labeled 4f, 5d–e_g,

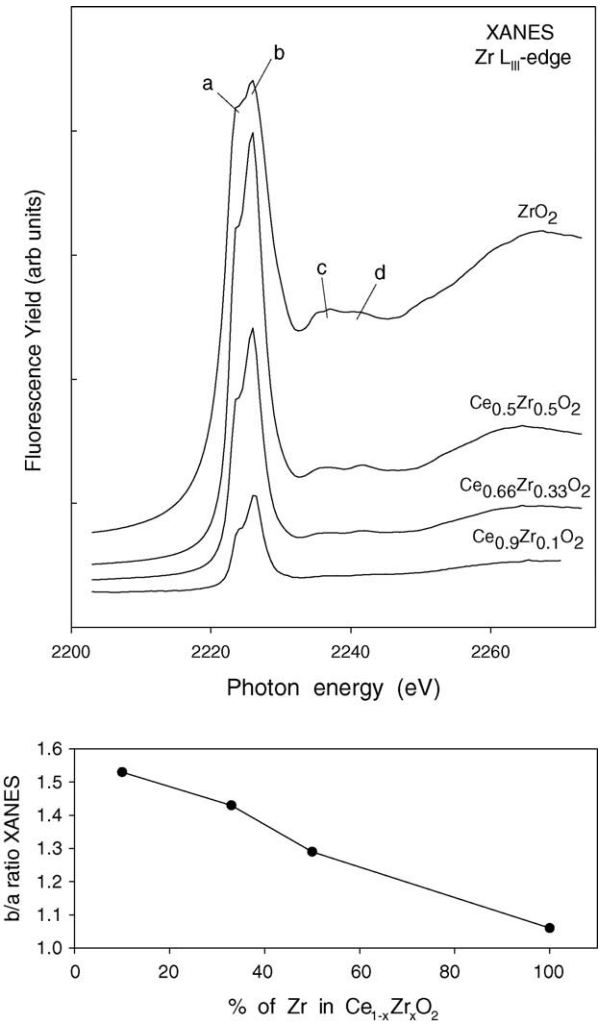

Fig. 4. Zr L_{III}-edge XANES spectra for bulk ZrO_2 and $Ce_{1-x}Zr_xO_2$ nanoparticles.

and 5d–t_{2g} in pure CeO_2 are related to electronic transitions from the O 1s core levels to the empty cerium 4f, 5de_g, and 5dt_{2g} levels, respectively [7,8]. The O K-edge spectrum of ZrO_2 comes mainly from O 1 s → Zr(4d) electronic transitions [18], and the two main peaks reflect the splitting of the Zr 4d orbitals into levels with e_g and t_{2g} symmetry [36]. The O K-edge spectra of the $Ce_{1-x}Zr_xO_2$ nanoparticles significantly change as a function of Zr doping. They exhibit features that match very well those found for $Ce_{1-x}Zr_xO_2$(1 1 1) surfaces [8]. The O K-edge spectra of $Ce_{1-x}Zr_xO_2$ compounds have a distinctive line shape that cannot be attributed to a sum of CeO_2 and ZrO_2 peaks. This is consistent with the results of DF calculations [8,17], which show Ce–O and Zr–O bond distances in $Ce_{1-x}Zr_xO_2$ not seen in the isolated oxides (i.e. some O atoms are in a special chemical environment).

Fig. 6 displays a series of valence band spectra for polycrystalline CeO_2, $Ce_{0.8}Zr_{0.2}O_2$(1 1 1) and Y-stabilized ZrO_2(1 1 1) [8]. Fig. 6A shows the typical valence spectrum of pure ceria [37]. For the fully oxidized CeO_2, no photoemission peaks exist between 0 and 4 eV within the band gap.

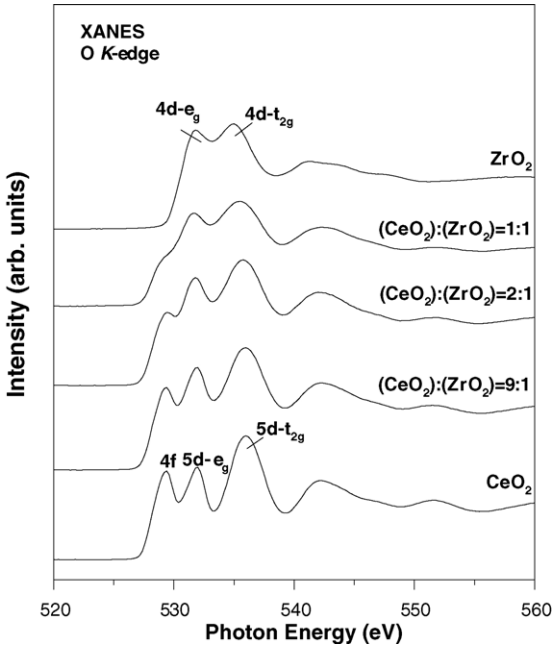

Fig. 5. O K-edge XANES spectra for bulk ZrO_2, $Ce_{1-x}Zr_xO_2$ nanoparticles, and bulk CeO_2.

The same is valid for the stoichiometric $Ce_{1-x}Zr_xO_2$ oxides [8,21]. Oxygen vacancies can be created by ion sputtering the $Ce_{1-x}Zr_xO_2(1\,1\,1)$ surfaces [8,21] or by reducing in hydrogen the $Ce_{1-x}Zr_xO_2$ nanoparticles [17]. The existence of O vacancies induces a new peak in the valence region (centered at ~2 eV, see Fig. 6). This peak is a Ce^{3+}-ion-derived level, related to occupied Ce $4f^1$ electronic states [37], and has a big impact on the chemical properties of the $Ce_{1-x}Zr_xO_{2-y}$ compounds [5,8,21].

3.3. Chemical properties of the $Ce_{1-x}Zr_xO_2$ systems

3.3.1. Reaction with hydrogen

In many situations, oxide catalysts are activated by partial reduction in hydrogen [38]. Hydrogen is one of the reducing agents in automotive exhaust gases [2,5]. The deviation of bulk ceria from its ideal CeO_2 composition has been extensively studied by temperature-programmed reduction (TPR) with hydrogen [39,40]. Similar experiments have also been carried out for bulk $Ce_{1-x}Zr_xO_2$ [4,5,32]. We found that $CeO_2(1\,1\,1)$ and $Ce_{1-x}Zr_xO_2(1\,1\,1)$ surfaces ($x < 0.4$) have a very low reactivity towards H_2. Fig. 7 shows typical photoemission data for the interaction of a $Ce_{1-x}Zr_xO_2(1\,1\,1)$ surface with hydrogen. In a reaction cell attached to a UHV

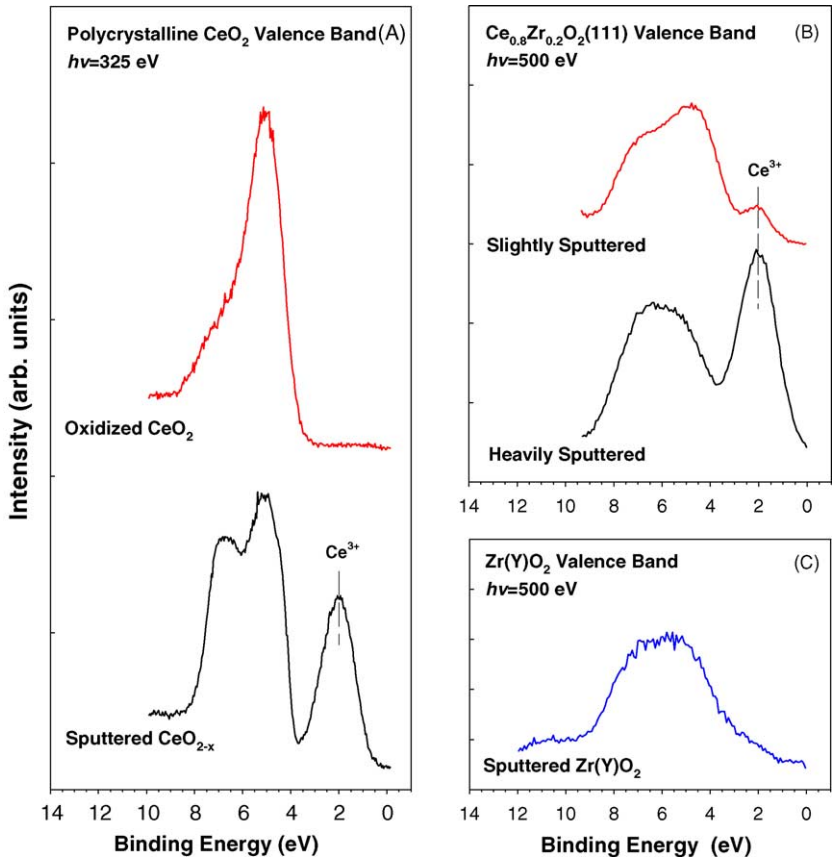

Fig. 6. Typical valence-band photoemission spectra for: (A) CeO_2 and CeO_{2-x}; (B) $Ce_{0.8}Zr_{0.2}O_{2-x}(1\,1\,1)$ with different defect populations, and (C) Y-stabilized $ZrO_{2-x}(1\,1\,1)$.

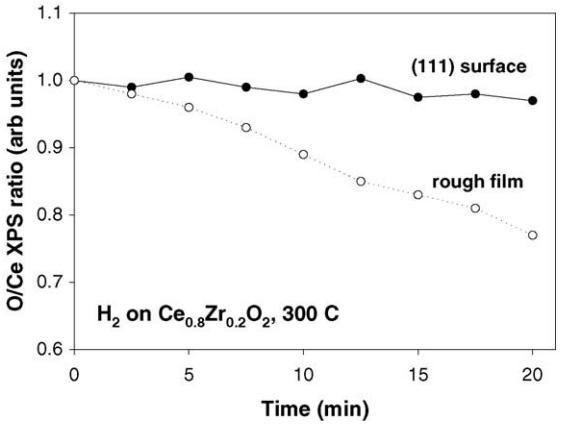

Fig. 7. O 1s/Ce 3d XPS ratio for a $Ce_{0.8}Zr_{0.2}O_2$(1 1 1) crystal and a rough $Ce_{0.8}Zr_{0.2}O_2$ film exposed to hydrogen (5 Torr of H_2, 300 °C) for different periods of time (see text).

chamber [41], the oxide surfaces were exposed to 5 Torr of H_2 at 300 °C for a given period of time. Then, the cell was pumped down ($< 5 \times 10^{-7}$ Torr) and the samples were transferred into the UHV chamber to measure the relative intensity of the O 1s and Ce 3d core levels. The data showed that at 300 °C essentially there was no reduction of the CeO_2(1 1 1) and $Ce_{1-x}Zr_xO_2$(1 1 1) surfaces. On the other hand, O removal was detected when similar experiments were done with rough films of CeO_2 or $Ce_{1-x}Zr_xO_2$ (see Fig. 7) and with $Ce_{1-x}Zr_xO_2$ nanoparticles. The presence of defects or imperfections in the surface of an oxide facilitates the reaction with hydrogen and the removal of O as gaseous water [41,42].

We investigated the partial reduction of the $Ce_{1-x}Zr_xO_2$ nanoparticles in a flow reactor using in situ time-resolved XRD and XANES [17]. Fig. 8 displays diffraction patterns obtained after heating $Ce_{0.9}Zr_{0.1}O_2$ nanoparticles from 25 to 1000 °C under a 5% H_2/95% He stream (20 cm^3/min). As the temperature increases, there is a narrowing of the diffraction peaks together with a clear shift in position. The narrowing indicates sintering of the nanoparticles (see above) and the shift to the lower angle in 2θ is a consequence of an expansion in their unit cell as a result of introducing O vacancies and/or sorbing hydrogen during the reduction process [17,39,40]. Water evolution was observed with a mass spectrometer located at the exit of the reaction cell [17]. Similar trends were observed in the corresponding XRD data for nanoparticles of CeO_2, $Ce_{0.5}Zr_{0.5}O_2$ and $Ce_{0.66}Zr_{0.33}O_2$. The diffraction results did not show the formation of reduced oxides with the crystal structures of $CeO_{1.71}$ or Ce_2O_3 [17,31]. However, XANES measurements at the Ce L_{III}-edge gave spectra with the line shape expected for a mixture of Ce^{4+} and Ce^{3+} [17,43]. Interestingly, there was no reduction of the Zr^{4+} cations [17].

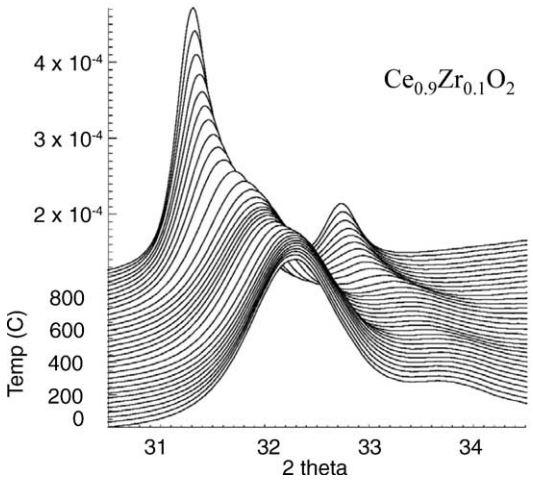

Fig. 8. Time-resolved XRD data for the heating of $Ce_{0.9}Zr_{0.1}O_2$ nanoparticles under a flow of 5% H_2/95% He. Heating rate = 5.9 °C/min. λ = 0.9034 Å.

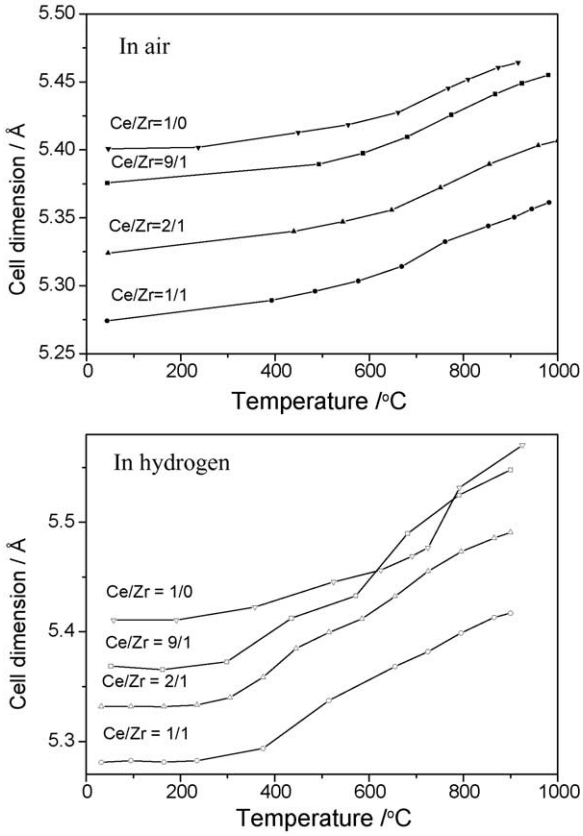

Fig. 9. Variations in cell dimension (Å) during annealing in air (top panel) and H_2-TPR (bottom panel) for a series of nanoparticles: $Ce_{0.5}Zr_{0.5}O_2$, $Ce_{0.66}Zr_{0.33}O_2$, $Ce_{0.90}Zr_{0.10}O_2$, and CeO_2. In the H_2-TPR experiments, the samples were heated under a flow (20 cm^3/min) of a 5% H_2/95% He mixture. Heating rate = 5.9 °C/min.

The bottom panel in Fig. 9 shows how the size of the unit cell of $Ce_{1-x}Zr_xO_2$ nanoparticles changes as a function of temperature when they are reduced in hydrogen. The cell expansions are much larger than seen during simple heating (compare to data in top panel of the figure)[1] as a consequence

[1] The cell dimensions obtained here taking into consideration asymmetry effects [31] are a little bit different (0.01–0.04 Å) from those obtained

of a chemical reaction (Ce^{3+} formation) and the sorption of hydrogen [17]. Substantial increases in cell dimension occur from 300 to 500 °C, and from 600 to 900 °C. It is clear that the CeO_2 nanoparticles exhibit the lowest reactivity towards H_2 in Fig. 9. This agrees with trends found in H_2-TPR experiments for bulk CeO_2 and $Ce_{1-x}Zr_xO_2$ [44], and it is frequently linked to the improvement in oxygen-storage capacity seen in Zr-doped ceria [45]. During the oxygen release process, there is stress in the oxide lattice as a consequence of the difference in atomic size of Ce^{4+} (0.97 Å) and Ce^{3+} (1.14 Å) [46]. The introduction of relatively small Zr^{4+} ions (0.84 Å) into the ceria framework could compensate the volume increment, and ease the valence change ($Ce^{4+} \rightarrow Ce^{3+}$) and reduction process in $Ce_{1-x}Zr_xO_2$ [45,46].

3.3.2. Adsorption and dissociation of SO_2

Ceria-based catalysts can be very useful for the destruction of SO_2 [6,7]. On the other hand, the SO_2 formed during the combustion of fuels in automotive engines can affect the performance of the CeO_2 or $Ce_{1-x}Zr_xO_2$ present in catalysts used for reducing CO and NO_x emissions [22]. The species responsible for ceria deactivation is mainly attributed to cerium sulfate, which blocks the Ce^{3+} sites for the redox cycle in the process of oxygen storage/release [22,47]. Reaction of SO_2 with CeO_2 powders and polycrystalline ceria films supported on Pt(1 1 1) at 25 °C shows sulfate (SO_4) as the main surface species as evidenced by a combination of XANES, temperature-programmed desorption (TPD), and high-resolution photoemission [7]. Photoemission studies for the adsorption of SO_2 on CeO_2(1 1 1) and $Ce_{1-x}Zr_xO_2$(1 1 1) point to the formation of a SO_x species on the surface that could be either SO_3 or SO_4 [21,48]. The identification of this species on the basis of only photoemission is not conclusive [21]. To address this issue, XANES was used to study the interaction of SO_2 with CeO_2(1 1 1) and $Ce_{1-x}Zr_xO_2$(1 1 1) surfaces. Fig. 10 shows S K-edge spectra for the adsorption of SO_2 on CeO_2(1 1 1) and $Ce_{0.7}Zr_{0.3}O_2$(1 1 1) surfaces at room temperature. A comparison to the corresponding peak positions for sulfates and sulfites [7,49] indicates that SO_4 is the main species formed on the oxide surfaces with a minor concentration of SO_3. There is no dissociation of the adsorbate.

The top layer of CeO_2(1 1 1) and $Ce_{0.7}Zr_{0.3}O_2$(1 1 1) contains only O atoms, see Fig. 1. The adsorption of SO_2 on these O atoms would yield directly sulfite or sulfate species:

$$SO_{2,\,gas} + O_{lattice} \rightarrow SO_{3,ads} \quad (1)$$

$$SO_{3,ads} + O_{lattice} \rightarrow SO_{4,ads} \quad (2)$$

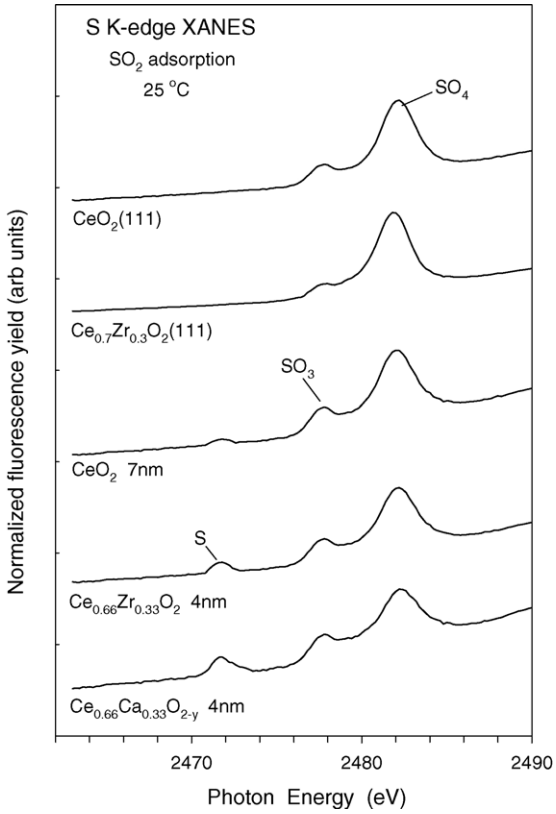

Fig. 10. S K-edge spectra taken after dosing SO_2 to CeO_2(1 1 1) and $Ce_{0.7}Zr_{0.3}O_2$(1 1 1) surfaces, and nanoparticles of CeO_2, $Ce_{0.66}O_{0.33}O_2$ and $Ce_{0.66}Ca_{0.33}O_{2-y}$. The samples were exposed to 0.1 Torr of SO_2, for 5 min at 25 °C.

There are "holes" in the top layer of CeO_2(1 1 1) and $Ce_{0.7}Zr_{0.3}O_2$(1 1 1) that expose Ce and Zr cations in the second layer, see Fig. 1. These cations have all their O neighbors (eight in total) and interact very weakly with an adsorbed SO_2 molecule [21]. One must introduce O vacancies in CeO_2(1 1 1) and $Ce_{0.7}Zr_{0.3}O_2$(1 1 1) to see the interaction of SO_2 with the metal cations and dissociation of the molecule [21,48].

In Fig. 10 are also shown S K-edge XANES spectra taken after exposing nanoparticles of CeO_2, $Ce_{0.66}Zr_{0.33}O_2$ and $Ce_{0.66}Ca_{0.33}O_{2-y}$ to SO_2 at 25 °C. Again one finds that SO_4 is the main sulfur-containing species present on the oxides but, in addition, features are seen at photon energies between 2470 and 2472 eV that denote the existence of metal–S bonds [7,49] as a consequence of the full dissociation of SO_2. In principle, clusters and nanoparticles of $Ce_{1-x}Zr_xO_2$ probably have metal cations at corner and edge sites (see Fig. 11 and refs. [10,18]) that can interact well with the SO_2 molecule. On some of these special sites that are very reactive SO_2 decomposes. In addition, there may be O vacancies in the surface of the $Ce_{0.66}Zr_{0.33}O_2$ and $Ce_{0.66}Ca_{0.33}O_{2-y}$ nanoparticles that facilitate S–O bond cleavage [21,48,49]. In Fig. 10, the $Ce_{0.66}Ca_{0.33}O_{2-y}$ system has the largest concentration of O vacancies [31,34], and the highest reactivity for the dissociation of SO_2.

ignoring asymmetry [17]. Independently of this, variations of the same order in the lattice dimension can be expected depending on the exact experimental procedure used for the preparation of the nanoparticles. In the case of $Ce_{0.5}Zr_{0.5}O_2$ nanoparticles, the coexistence of an almost cubic phase and a trace of a tetragonal phase could occur. The reported values are for the cubic or pseudo-cubic phase.

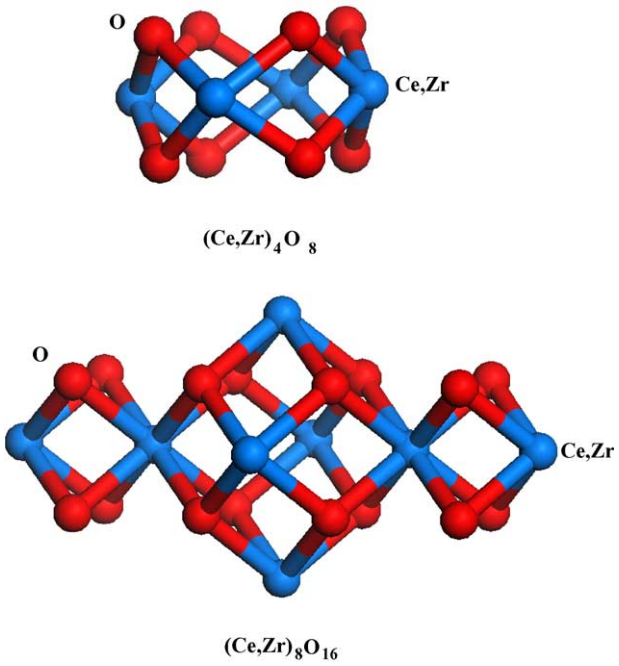

Fig. 11. Possible structures for nanoclusters of CeO_2 or $Ce_{1-x}Zr_xO_2$. Even for stoichiometric systems, corner and edge atoms that have a low coordination number can exist.

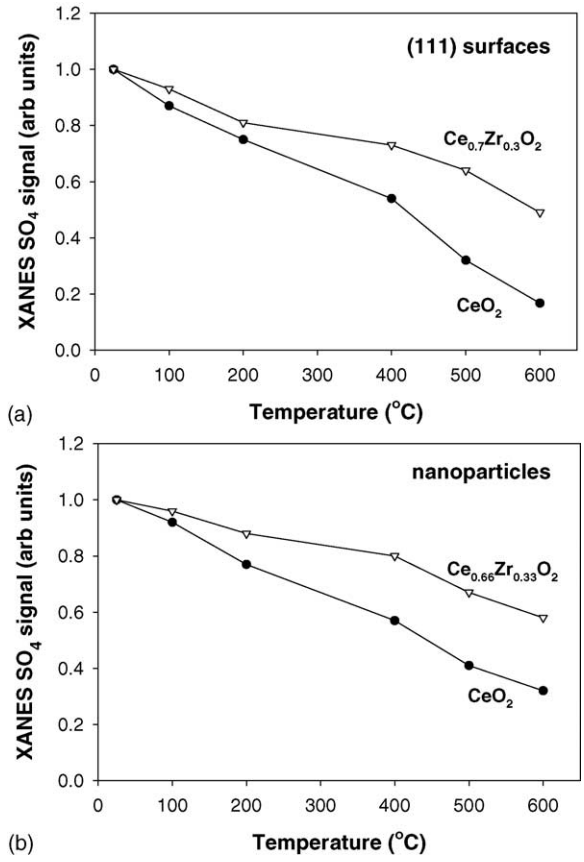

Fig. 12. Effect of temperature on the XANES signal for the SO_4 formed on the CeO_2 and $Ce_{1-x}Zr_xO_2$ systems of Fig. 10. The top panel shows the results for the (1 1 1) surfaces, while the bottom panel contains the corresponding results for the nanoparticles.

Fig. 12 shows the effect of the temperature on the sulfate (SO_4) signal for the CeO_2 and $Ce_{1-x}Zr_xO_2$ systems in Fig. 10. As the temperature is raised SO_4 decomposes. In the case of the CeO_2(1 1 1) and $Ce_{0.7}Zr_{0.3}O_2$(1 1 1) surfaces, the adsorbed SO_4 transforms into SO_2 gas. On the other hand, in the case of the nanoparticles, most of the decomposed SO_4 yields SO_2 gas, but a fraction undergoes complete decomposition depositing S on the oxide substrate. The SO_4 adsorbed on the nanoparticles is somewhat more stable than that present on the (1 1 1) surfaces. For both types of systems, the presence of Zr seems to induce an increase in the thermal stability of the adsorbed sulfate. The Zr cations also enhance the thermal stability of SO_4 species formed on partially reduced $Ce_{1-x}Zr_xO_{2-y}$(1 1 1) surfaces [21].

4. Summary and conclusions

Synchrotron-based techniques (high-resolution photoemission, time-resolved X-ray diffraction, and X-ray absorption near-edge spectroscopy) were used to investigate the physical and chemical properties of $Ce_{1-x}Zr_xO_2$(1 1 1) surfaces and $Ce_{1-x}Zr_xO_2$ particles with sizes between 4 and 7 nm. The results of XANES (O K-edge, Ce and Zr L_{III}-edges) indicate that the $Ce_{1-x}Zr_xO_2$ nanoparticles and $Ce_{1-x}Zr_xO_2$(1 1 1) surfaces have very similar electronic properties. For these systems, the lattice constant decreased with increasing Zr content, varying from 5.4 Å in CeO_2 to 5.3 Å in $Ce_{0.5}Zr_{0.5}O_2$. Within the fluorite structure, the Zr atoms exhibited structural perturbations that led to different types of Zr–O distances and non-equivalent O atoms in the $Ce_{1-x}Zr_xO_2$ compounds. Their Zr L_{III}- and O K-edge XANES spectra displayed features not seen in pure ZrO_2 or CeO_2.

The $Ce_{1-x}Zr_xO_2$ nanoparticles were more reactive towards H_2 and SO_2 than the $Ce_{1-x}Zr_xO_2$(1 1 1) surfaces. The $Ce_{1-x}Zr_xO_2$(1 1 1) surfaces did not reduce in hydrogen at 300 °C. At temperatures above 250 °C, the $Ce_{1-x}Zr_xO_2$ nanoparticles reacted with H_2 and water evolved into gas phase. XANES showed the generation of Ce^{3+} cations without reduction of Zr^{4+}. There was an expansion in the unit cell of the reduced nanoparticles probably as a consequence of a partial $Ce^{4+} \rightarrow Ce^{3+}$ transformation and the sorption of hydrogen into the bulk of the material. S K-edge XANES spectra pointed to SO_4 as the main product of the adsorption of SO_2 on the $Ce_{1-x}Zr_xO_2$ nanoparticles and $Ce_{1-x}Zr_xO_2$(1 1 1) surfaces. Full dissociation of SO_2 was seen on the nanoparticles but not on the $Ce_{1-x}Zr_xO_2$(1 1 1) surfaces. The metal cations at corner and edge sites of the $Ce_{1-x}Zr_xO_2$ nanoparticles probably play a very important role in interactions with the H_2 and SO_2 molecules.

Acknowledgements

The research carried out at Brookhaven National Laboratory and Pacific Northwest National Laboratory was financed

by the US Department of Energy (DOE), Office of Basic Energy Sciences, Division of Chemical Sciences. Work at the "Instituto de Catálisis (CSIC)" was done with financial support from CICYT (project MAT2000-1467). The National Synchrotron Light Source is supported by the Divisions of Materials and Chemical Sciences of DOE. A portion of the work was performed in the Environmental Molecular Sciences Laboratory (EMSL), a national scientific user facility located at Pacific Northwest National Laboratory and supported by the DOE Office of Biological and Environmental Research.

References

[1] J.M. Thomas, W.J. Thomas, Principles and Practice of Heterogeneous Catalysis, VCH, New York, 1997.
[2] M. Shelef, R.W. McCabe, Catal. Today 62 (2000) 35.
[3] K.C. Taylor, Catal. Rev. Sci. Eng. 35 (1993) 457.
[4] M. Fernández-García, A. Martínez-Arias, A. Iglesias-Juez, A.B. Hungría, J.A. Anderson, J.C. Conesa, J. Soria, Appl. Catal. B: Environ. 31 (2001) 39.
[5] A. Trovarelli, Catal. Rev. Sci. Eng. 38 (1996) 439.
[6] T. Zhu, L. Kundakovic, A. Dreher, M. Flytzani-Stephanopoulos, Catal. Today 50 (1999) 381.
[7] J.A. Rodriguez, T. Jirsak, A. Freitag, J.C. Hanson, J.Z. Larese, S. Chaturvedi, Catal. Lett. 62 (1999) 113.
[8] G. Liu, J.A. Rodriguez, J. Hrbek, J. Dvorak, C.H.F. Peden, J. Phys. Chem. B 105 (2001) 7762.
[9] J. Stubenrauch, J.M. Vohs, J. Catal. 159 (1996) 50.
[10] H. Cordatos, D. Ford, R. Gorte, J. Phys. Chem. 100 (1996) 18128.
[11] S. de Carolis, J.L. Pascual, L.G.M. Petterson, M. Baudin, M. Wojcik, K. Hermansson, A.E.C. Palmqvist, M. Muhammed, J. Phys. Chem. B 103 (1999) 7627.
[12] G. Balducci, M. Islam, J. Kašpar, P. Fornasiero, M. Graziani, Chem. Mater. 12 (2000) 677.
[13] J.A. Rodriguez, Theor. Chem. Acc. 107 (2002) 117.
[14] F. Zhang, S.-W. Chan, J.E. Spanier, E. Apak, Q. Jin, R.D. Robinson, I.P. Herman, Appl. Phys. Lett. 80 (2002) 127.
[15] E.S. Putna, T. Bunluesin, X.L. Fan, R.J. Gorte, J.M. Vohs, R.E. Lakis, T. Egami, Catal. Today 50 (1999) 343.
[16] S. Rossignol, Y. Madier, D. Duprez, Catal. Today 50 (1999) 261.
[17] J.A. Rodriguez, J.C. Hanson, J.-Y. Kim, G. Liu, A. Iglesias-Juez, M. Fernández-García, J. Phys. Chem. B 107 (2003) 3535.
[18] M. Fernández-García, A. Martínez-Arias, J.C. Hanson, J.A. Rodriguez, Chem. Rev. 104 (2004) 4063.
[19] A. Martínez-Arias, M. Fernández-García, V. Ballesteros, L.N. Salamanca, J.C. Conesa, C. Otero, J. Soria, Langmuir 15 (1999) 4796.
[20] M. Fernández-García, A. Martínez-Arias, A.B. Hungría, A. Iglesias-Juez, J.C. Conesa, J. Soria, Phys. Chem. Chem. Phys. 4 (2002) 2473.
[21] G. Liu, J.A. Rodriguez, Z. Chang, J. Hrbek, C.H.F. Peden, J. Phys. Chem. B 108 (2004) 2931.
[22] R.M. Ferrizz, R.J. Gorte, J.M. Vohs, Catal. Lett. 82 (2002) 123.
[23] Y.J. Kim, S. Thevuthasan, V. Shutthananadan, C.L. Perkins, D.E. McCready, G.S. Herman, Y. Gao, T.T. Tran, S.A. Chambers, C.H.F. Peden, J. Electron Spectrosc. Relat. Phenom. 126 (2002) 177.
[24] V. Shutthanandan, S. Thevuthasan, Y.J. Kim, C.H.F. Peden, Mater. Res. Soc. Symp. Proc. 654 (2001) AA2.6/1.
[25] P. Norby, J. Hanson, Catal. Today 39 (1998) 301, and references therein.
[26] A.P. Hammersely, S.O. Svensson, A. Thompson, Nucl. Instrum. Methods Phys. Res. 346 (1994) 321.
[27] A.C. Larson, R.B. von Dreele, GSAS General Structure Analysis System, Report LAUR 86-748, Los Alamos National Laboratory, Los Alamos, NM, 1995.
[28] P. Norby, F.I. Pashni, A.F. Gualtieri, J.C. Hanson, C.P. Grey, J. Phys. Chem. B 102 (1998) 839.
[29] P. Thompson, D.E. Cox, J.B. Hastings, J. Appl. Cryst. 20 (1987) 79.
[30] J. Baldinozzi, J.F. Berar, J. Appl. Cryst. 26 (1993) 128.
[31] X. Wang, J.C. Hanson, G. Liu, J.A. Rodriguez, A. Iglesias-Juez, M. Fernández-García, J. Chem. Phys. 121 (2004) 5434.
[32] P. Fornasiero, E. Fonda, R. Di Monte, G. Vlaic, J. Kašpar, M. Graziani, J. Catal. 187 (1999) 177.
[33] R. Jenkins, R.L. Snyder, Introduction to X-ray Powder Diffractometry, Wiley, New York, 1996, p. 91.
[34] J.A. Rodriguez, X. Wang, J.C. Hanson, G. Liu, A. Iglesias-Juez, M. Fernández-García, J. Chem. Phys. 119 (2003) 5659.
[35] A. Christensen, E.A. Carter, Phys. Rev. B 58 (1998) 8050.
[36] N. Thromat, C. Noguera, M. Gautier, F. Jollet, J.P. Duraud, Phys. Rev. B 44 (1991) 7904.
[37] D.R. Mullins, S.H. Overbury, D. Huntley, Surf. Sci. 409 (1998) 307.
[38] H.H. Kung, Transition Metal Oxides: Surface Chemistry and Catalysis, Elsevier, New York, 1989.
[39] K. Sohlberg, S.K. Pantelides, S.J. Pennycook, J. Am. Chem. Soc. 123 (2001) 6609, and references therein.
[40] J.L.G. Fierro, J. Soria, J. Sanz, J.M. Rojo, J. Solid State Chem. 66 (1987) 154.
[41] J.Y. Kim, J.A. Rodriguez, J.C. Hanson, A. Frenkel, P.L. Lee, J. Am. Chem. Soc. 125 (2003) 10685.
[42] J.A. Rodriguez, J.C. Hanson, A.I. Frenkel, J.Y. Kim, M. Pérez, J. Am. Chem. Soc. 124 (2002) 346.
[43] S.H. Overbury, D.R. Huntley, D. Mullins, G.N. Cleave, Catal. Lett. 51 (1998) 133, and references therein.
[44] G. Vlaic, R. Di Monte, P. Fornasiero, E. Fonda, J. Kašpar, M. Graziani, J. Catal. 182 (1999) 378.
[45] G. Balducci, J. Kašpar, P. Fornasiero, M. Granziani, M.S. Islam, J.D. Gale, J. Phys. Chem. B 101 (1997) 1750.
[46] Y. Nagai, T. Yamamoto, T. Tanaka, S. Yoshida, T. Nonaka, T. Okamoto, A. Suda, M. Sugiura, Catal. Today 74 (2002) 225.
[47] W. Waqif, P. Bazin, O. Saur, J.C. Lavalley, G. Balanchard, O. Touret, Appl. Catal. B 11 (1997) 193.
[48] S.H. Overbury, D.R. Mullins, D. Huntley, L.J. Kundakovic, J. Phys. Chem. B 103 (1999) 11308.
[49] J.A. Rodriguez, T. Jirsak, L. González, J. Evans, M. Pérez, A. Maiti, J. Chem. Phys. 115 (2001) 10914.